PHYSICAL REVIEW E **68**, 036305 (2003)

Periodic folding of viscous sheets

Neil M. Ribe
UMR 7579 CNRS, Institut de Physique du Globe, 4 place Jussieu, 75252 Paris Cédex 05, France

(Received 28 April 2003; published 9 September 2003)

The periodic folding of a sheet of viscous fluid falling upon a rigid surface is a common fluid mechanical instability that occurs in contexts ranging from food processing to geophysics. Asymptotic thin-layer equations for the combined stretching-bending deformation of a two-dimensional sheet are solved numerically to determine the folding frequency as a function of the sheet's initial thickness, the pouring speed, the height of fall, and the fluid properties. As the buoyancy increases, the system bifurcates from ''forced'' folding driven kinematically by fluid extrusion to ''free'' folding in which viscous resistance to bending is balanced by buoyancy. The systematics of the numerically predicted folding frequency are in good agreement with laboratory experiments.

DOI: 10.1103/PhysRevE.68.036305 PACS number(s): 47.20.Gv, 47.15.Gf, 47.20.Bp

A sheet of viscous fluid poured from a sufficient height approaches a surface not directly, but rather in the form of periodic folds (Fig. 1). In a home kitchen, the phenomenon is easily reproduced using honey, cake batter, or molten chocolate. The same instability is observed during the commercial filling of food containers [1] and in polymer processing [2], and may occur in the earth when subducted oceanic lithosphere encounters discontinuities in viscosity and density at 660 or 2900 km depth [3]. Yet despite its importance, periodic folding of viscous sheets has proved surprisingly resistant to theoretical explanation. The first major step forward was Taylor's suggestion [4] that fluid folding, like its elastic analog, requires a longitudinal compressive stress. Subsequently, systematic experiments were carried out on the periodic folding of sheets incident on rigid surfaces [5,6] and on density-viscosity interfaces [3]. Additional theoretical insight has been provided by linear stability analysis of incipient folding [7,8] and by numerical simulations of finite-amplitude folding using a marker-and-cell approach [1] or inextensible thin-layer theory [9]. Finally (nontime periodic) viscous folding has been studied in a variety of other geometries, such as shear-induced buckling of flat layers [10,11] and axisymmetric folding of spherical [12] or conical [13] sheets. The present study extends earlier work on periodic viscous folding by identifying a previously unrecognized bifurcation, proposing a complete scaling law for the folding frequency, and comparing the predictions of the latter with experimental observations.

In this paper we study a simple model for periodic viscous folding that corresponds as closely as possible to the standard laboratory setup [5]: a two-dimensional sheet with constant viscosity μ, buoyancy ρg, and surface tension coefficient γ, extruded downward at speed U_0 from a slot of width H_0 toward a rigid plate a distance L below the slot. Let the sheet's thickness be $H(s,t)$, where s is arclength along the sheet's midsurface and t is time. If $\mathbf{r}(s,t)$ be the Cartesian coordinates of a point on the midsurface, then $\mathbf{s}\equiv\partial\mathbf{r}/\partial s$ is a unit vector parallel to the midsurface. Let $\mathbf{z}$ be the unit vector normal to $\mathbf{s}$, $\theta(s,t)$ be the inclination of the midsurface from the horizontal, and $K(s,t)\equiv\partial\theta/\partial s$ be the midsurface curvature.

The equations governing the dynamics of the sheet comprise a set of six equations that describe its mechanical response to applied loads, together with kinematic equations that describe how the sheet's geometry and thickness change with time. Under the assumption that fluid inertia is negligible, the mechanical equations are [14,15]

$$\frac{\partial N}{\partial s}=KQ+\rho gH\sin\theta, \tag{1a}$$

$$\frac{\partial Q}{\partial s}=-KN+\rho gH\cos\theta-2\gamma K, \tag{1b}$$

$$\frac{\partial M}{\partial s}=Q, \tag{1c}$$

$$\frac{\partial W}{\partial s}=\omega-KU, \tag{1d}$$

$$\frac{\partial U}{\partial s}=KW+\frac{1}{4\mu H}\left(N-\frac{5}{2}KM\right), \tag{1e}$$

$$\frac{\partial\omega}{\partial s}=-\frac{3M}{\mu H^3}. \tag{1f}$$

Here $U\mathbf{s}+W\mathbf{z}$ is the local velocity of the sheet's midsurface and ω is its local rate of rotation. The stress resultants N and Q and the bending moment M are defined by

$$(N,Q,M)=\int_{-H/2}^{H/2}(\sigma_{ss},\sigma_{sz},z\sigma_{ss})dz, \tag{2}$$

where σ_{ss} and σ_{sz} are the extensional and shear components of the stress tensor, respectively. Equations (1) comprise a sixth-order system of ordinary differential equations, which describes the instantaneous (quasistatic) response of a sheet with a given geometry to applied loads. Equations (1a) and (1b) describe the global (integrated across the sheet) force balances in the $\mathbf{s}$ and $\mathbf{z}$ directions, respectively, and Eq. (1c) describes the global torque balance. Equation (1d) is just a

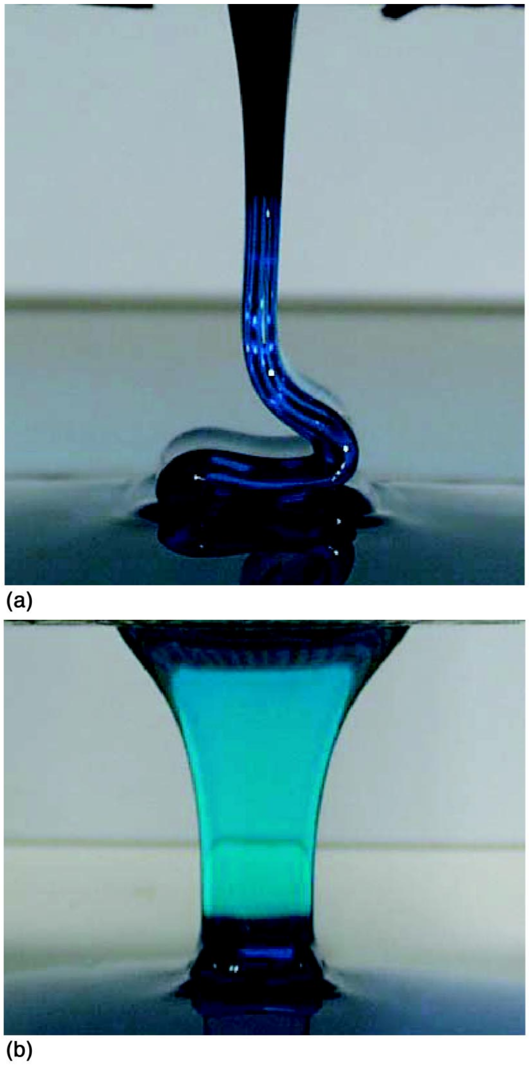

FIG. 1. Periodic folding of a sheet of glucose syrup with viscosity $\mu = 120$ Pa s, viewed parallel to (a) and normal to (b) the sheet. The height of fall is 7.0 cm, and the dimensions of the extrusion slot are 0.7 cm×5.0 cm. Photographs by the author.

definition of the rotation rate ω. Equations (1e) and (1f) are constitutive relations for N and M, respectively.

The kinematic equations governing changes of the sheet's geometry are [14,16]

$$\frac{\mathcal{D}\mathbf{r}}{\mathcal{D}t} = U\mathbf{s} + W\mathbf{z}, \tag{3a}$$

$$\frac{\mathcal{D}\theta}{\mathcal{D}t} = \omega, \tag{3b}$$

$$\frac{\mathcal{D}K}{\mathcal{D}t} = \frac{\partial \omega}{\partial s} - K\Delta, \tag{3c}$$

$$\frac{\mathcal{D}H}{\mathcal{D}t} = -H\Delta, \tag{3d}$$

where

$$\frac{\mathcal{D}}{\mathcal{D}t} \equiv \frac{\partial}{\partial t} + \left(U_0 + \int_0^s \Delta\, ds \right) \frac{\partial}{\partial s} \equiv \frac{\partial}{\partial t} + V \frac{\partial}{\partial s} \tag{4}$$

is a convective derivative that follows the motion of material points on the sheet's midsurface and

$$\Delta = \frac{\partial U}{\partial s} - KW \tag{5}$$

is the rate of stretching of the midsurface.

The six boundary conditions at the ends of the sheet are obtained from the assumption that the sheet is "clamped" at both ends, i.e., its rotation rate and its velocity (relative to that imposed at the end in question) are zero there. This requires

$$U(0,t) - U_0 = W(0,t) = \omega(0,t) = U(\ell,t) = W(\ell,t) - \tfrac{1}{2}\cos\theta(\ell,t)\dot{H}(\ell,t) = \omega(\ell,t) = 0. \tag{6}$$

where the extrusion slot is at $s = 0$ and $\ell(t)$ is the (unknown) length of the sheet. The condition on $W(\ell,t)$ takes into account the component of vertical velocity due to changes in the sheet's thickness at the contact line, where the dot denotes the (total) time derivative. Appendix I shows that three types of contact line are possible, depending on the curvature $K(\ell,t) \equiv K_c$ at the contact and its rate of change. When $K_c \neq 0$, the contact line is fixed; but two distinct cases must be distinguished. The contact line is "pinned" when the (absolute) curvature there is increasing $(d|K_c|/dt > 0)$, which will occur when the forces acting on the sheet are such as to tend to peel it away from the plate. The contact line does not move in this case because a portion of the sheet already laid down adheres to the plate and cannot be peeled off again. The contact line is "relaxing" when the curvature there is decreasing $(d|K_c|/dt < 0)$, which will occur if the applied forces push the portions of the sheet near the contact towards the plate. Finally, if the relaxation continues until K_c vanishes, the contact line becomes a "mobile" one, maintaining zero curvature while moving laterally with a velocity

$$-\frac{d\omega}{dK}(\ell,t)\mathbf{s}(\ell,t) \equiv U_c \mathbf{s}(\ell,t). \tag{7}$$

The numerical code used in this study was specially designed to track accurately through time the changing character of the contact line.

By nondimensionalizing the governing equations and end conditions using L, U_0, and L/U_0 as scales for length, velocity, and time, respectively, one finds that the sheet's dynamics are controlled by the values of three dimensionless groups: the slenderness $\epsilon = H_0/L$; the buoyancy number $B = \rho g L^2/\mu U_0$ (buoyancy/viscous force); and the inverse capillary number $S = \gamma/\mu U_0$ (surface tension/viscous force.) Consider first what the governing equations imply about the scaling of periodic folding in the absence of surface tension $(S = 0)$. Figure 1(a) shows that the sheet generally exhibits a bipartite structure comprising a nearly vertical "tail" above a smaller region in which the folding occurs. Deformation in the tail is by steady-state extension under gravity, which reduces the sheet's thickness from H_0 at the extrusion slot to some smaller value H_1 (say) where the fluid enters the folding region. The fluid velocity at the latter point is just that required by steady-state volume conservation in the tail, or $U_1 = H_0 U_0 / H_1$.

Neglecting for the moment the (relatively small) effect of surface tension, we anticipate the possibility of two distinct scalings for the folding amplitude δ and frequency $f \sim U_1/\delta$, depending on the importance of buoyancy forces. The first occurs when buoyancy is negligible, and folding is driven entirely by extrusion of fluid from the slot ("forced" folding). Because stretching is negligible, $H_0 \approx H_1$ and $U_0 \approx U_1$. Moreover, the governing equations are homogeneous, so neither δ nor f can depend on either μ or H_1 (although the force required to extrude the fluid will still depend on these). Dimensional considerations then require

$$\delta \sim L, \quad f \sim \frac{U_1}{L}. \tag{8}$$

The second scaling is for "free" folding, in which bending resistance in the folding region is balanced by buoyancy. This balance is expressed by eliminating Q and M from Eq. (1b), using Eqs. (1c) and (1f) and noting that $H \approx H_1$ is nearly constant in the folding region, which implies

$$\frac{\mu H_1^3}{3} \frac{\partial^3 \omega}{\partial s^3} \sim H_1 g \cos\theta. \tag{9}$$

Because $\partial/\partial s \sim \delta^{-1}$ and $\omega \sim U_1/\delta$, Eq. (9) implies

$$\delta \sim \left(\frac{\mu H_1^2 U_1}{\rho g} \right)^{1/4}, \quad f \sim \left(\frac{\rho g U_1^3}{\mu H_1^2} \right)^{1/4}. \tag{10}$$

The above scaling was previously proposed by Ref. [9].

To demonstrate the existence of the above limits and to map out the transition between them, I have written a Lagrangian numerical code that follows the motion of material points on the sheet's midsurface. Each numerical time step comprises two distinct parts. Given a sheet with a specified geometry, the code first solves a sixth-order two-point boundary-value problem [Eqs. (1)] for the instantaneous flow within the sheet using the (second-order accurate) relaxation algorithm of Ref. [17]. Kinematic equations (3) are then solved using a second-order Runge-Kutta (midpoint) method to advance the geometry forward in time. The initial geometry of the sheet comprises a vertical tail of adjustable length above a small arc-shaped part whose end is tangent to the plate. Time stepping is continued until a steady periodic state is reached. To avoid fold "pile-up," the portion of the sheet downstream of the contact line is instantaneously removed, each time a new contact is formed [9]. The total number of material points in the sheet thus changes continuously: a new point is added at the extrusion slot at each time step, whereas points are removed when a new contact line forms or an existing one moves.

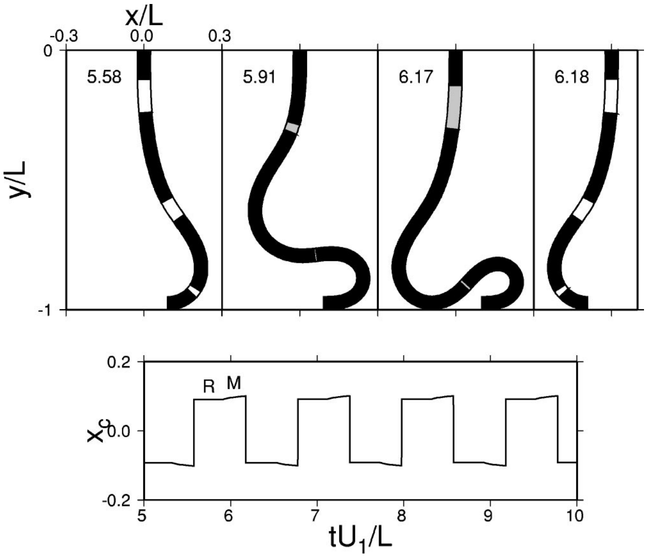

FIG. 2. Forced folding with $\epsilon^{-1} = 20$, $B = 0.1$, and $S = 0$ (no surface tension). The four upper panels show the changing shape of the sheet over a half-period of the oscillation, at the dimensionless times tU_1/L indicated at upper left in each panel. Colors denote the type of deformation that accounts for $>50\%$ of the local energy dissipation rate: extension (gray), shortening (white), and bending (black.) The lower panel shows the lateral position x_c of the contact line as a function of time. Relaxing and mobile contact lines are denoted by R and M, respectively.

Figures 2 and 3 show the evolution of the sheet's geometry and the position $x_c(t)$ of its contact line for two cases: forced folding with $\epsilon^{-1} = 20$ and $B = 0.1$ (Fig. 2), and free folding with $\epsilon^{-1} = 10$ and $B = 50$ (Fig. 3). Values of the dimensionless time tU_1/L are shown at the upper left of each of the four panels in the top row, which span a half-period of the oscillation. The third panel in each figure shows the formation of a new contact point and the fourth shows the sheet just after the portion downstream from the new contact has been removed. Colors indicate the type of deformation that accounts for 50% or more of the local rate of viscous dissi-

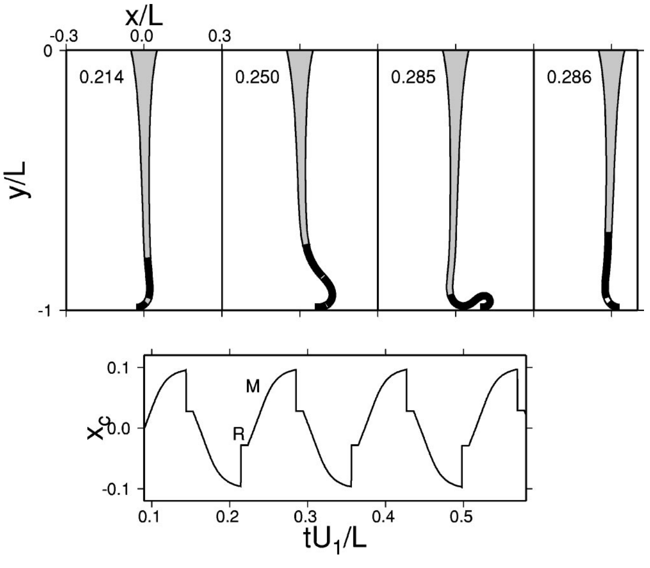

FIG. 3. Same as Fig. 2, but for free folding with $\epsilon^{-1} = 10$ and $B = 50$.

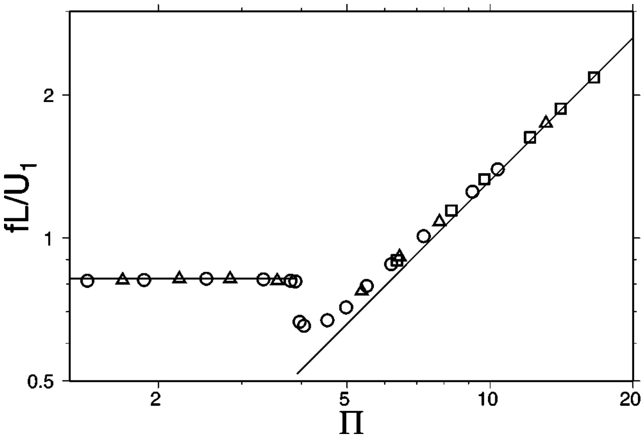

FIG. 4. Dimensionless folding frequency fL/U_1 as a function of Π [Eq. (11)], for 29 numerical solutions of the thin-sheet equations (1) and (3) with $S=0$ (no surface tension.) Results are shown for $\epsilon^{-1}=10$ (squares), 20 (circles), and 40 (triangles), with $0.005 \leqslant B \leqslant 100$. Solid lines are $fL/U_1=0.821$ (left) and $fL/U_1=0.132\Pi$ (right).

pation: extension (gray), compression (white), or bending (black). Deformation in forced folding is dominated by bending everywhere except at inflexion points. In free folding, by contrast, the sheet consists of a long extensional tail above a smaller bending-dominated region. Forced and free folding are also distinguished by the behavior of the respective contact lines. In forced folding in the limit $B=0$, the contact line is always a relaxing one (R). In Fig. 2, however, the small amount of buoyancy present $(B=0.1)$ causes the contact line to relax faster and eventually to become mobile (M). In free folding, by contrast, buoyancy is so strong that the contact line is mobile most of the time, with only short periods of relaxation after the formation of new contacts. Pinned contact lines never occurred in any of the numerical solutions.

The control parameter that governs the transition from forced to free folding is obtained by noting that their respective frequencies (8) and (10) are of the same order when the dimensionless parameter

$$\Pi=\left(\frac{\rho g L^4}{\mu U_0 H_0 H_1}\right)^{1/4} \tag{11}$$

is of order unity. If the scaling analysis is correct, a log-log plot of fL/U_1 vs Π should define straight lines with slopes of either zero (forced folding) or unity (free folding). Figure 4 shows such a plot for 29 numerical solutions with $S=0$ and various values of ϵ and B. Forced folding occurs when the buoyancy is less than a critical value $\Pi \approx 3.92 \pm 0.04$, at which point a bifurcation to a state of free folding occurs. The free-folding branch achieves its "pure" asymptotic form $fL/U_1 \approx 0.132\Pi$ for $\Pi \geqslant 10$. The single-valuedness of the curve in Fig. 4 was tested by varying the initial conditions for fixed values of ϵ and B. In all cases, the same final state was reached, suggesting (but admittedly not proving) that other stable forced- and free-folding branches with different frequencies do not exist.

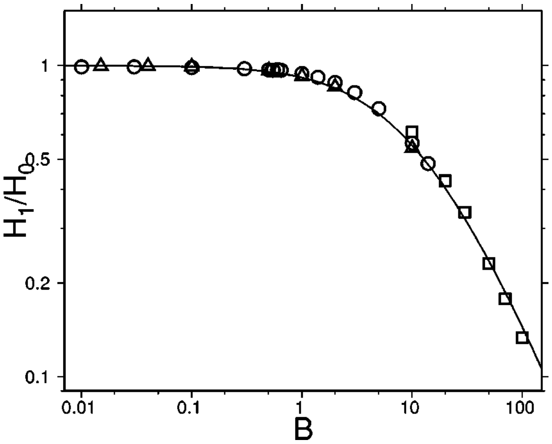

FIG. 5. H_1/H_0 vs B for the 29 numerical solutions of Fig. 3. Solid line is the exact solution of Eq. (12) with $\hat{s}_1=0.88$.

It remains to determine how the sheet thickness H_1 in the folding region depends on the external parameters ϵ and B. The thickness H_1 is a measure of the total amount of stretching that occurs in the tail of the sheet (gray portion of Fig. 3.) While the lower part of the sheet undergoes periodic folding, the tail remains nearly vertical and in a steady state, deforming by stretching alone with negligible bending. The flow in the tail is thus governed by Eqs. (1a) and (1e) with $W=Q=M=0$, $\theta=3\pi/2$, and $U=U_0H_0/H$, or

$$\left(\frac{H'}{H}\right)'=\frac{\rho g}{4\mu U_0 H_0}H, \tag{12}$$

where primes denote differentiation with respect to s. The boundary conditions are $H(0)-H_0=H'(s_1)=0$, where $s_1<L$ is the total length of the tail. The solution of Eq. (12) that satisfies $H'(s_1)=0$ is

$$H(s)=H_1\sec^2\left[\left(\frac{BH_1}{2H_0}\right)^{1/2}\left(\frac{s-s_1}{2L}\right)\right], \tag{13}$$

from which H_1 can be found by solving numerically the transcendental equation $H(0)=H_0$. In the limit $B \gg 1$,

$$\frac{H_1}{H_0}=2\pi^2\hat{B}^{-1}[1-4\sqrt{2}\hat{B}^{-1/2}+24\hat{B}^{-1}+O(\hat{B}^{-3/2})], \tag{14}$$

where $\hat{B}=B(s_1/L)^2$. Note that the function $H_1(B)$ is a power law $(H_1 \sim H_0 B^{-1})$ only in the limit $B \rightarrow \infty$; this result will be seen below to explain a significant feature of Cruickshank's experimental data [5]. Figure 5 shows that the calculated dependence of H_1/H_0 on B for the 29 numerical solutions agrees closely with the analytical solution for $s_1/L=0.88$ (solid line). This implies that the height of the folding portion of the sheet is about $0.12L$ on average.

Combining the results of Figs. 4 and 5, one obtains a complete scaling law for the folding frequency in terms of the known input parameters:

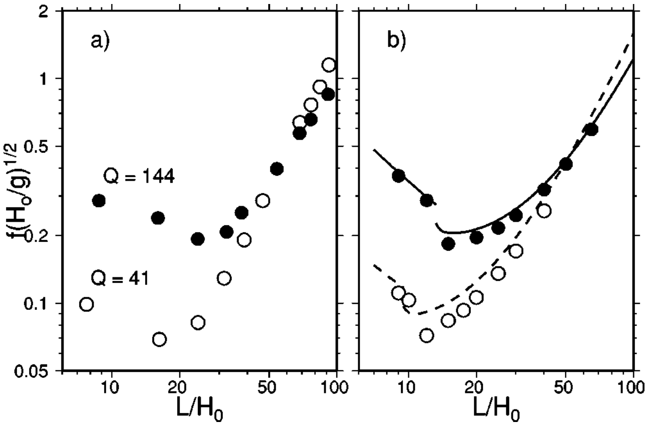

FIG. 6. (a) Experimentally measured folding frequencies [5] for viscous sheets with $S^\star \equiv \gamma/\rho g H_0^2 = 0.59$ and $Q \equiv \mu U_0/\rho g H_0^2 = 41$ (open circles) and $Q = 144$ (solid circles). (b) Numerically predicted folding frequencies for the same values of $S^\star$ and Q (circles), together with the scaling law (15) (dashed lines for $Q = 41$ and solid lines for $Q = 144$). The rightmost circles are at the largest values of ϵ^{-1} for which numerical solutions could be obtained.

$$f = \frac{U_0}{L F_2(B)} F_1\left[\left(\frac{B}{\epsilon^2 F_2(B)}\right)^{1/4}\right], \tag{15}$$

where F_1 and F_2 are the functions shown in Fig. 4 and Fig. 5, respectively. The "nested" structure of Eq. (15) reflects the fact that the sheet thickness H_1 in the folding region, upon which the folding frequency f depends by Eq. (10), is itself controlled by a different process (stretching) that occurs elsewhere (in the tail).

The numerical predictions can be compared directly with the experimental observations of Cruickshank [5], who measured the dimensionless frequency $f(H_0/g)^{1/2}$ as a function of the dimensionless height of fall $L/H_0 \equiv \epsilon^{-1}$ for fixed values of H_0, the dimensionless flow rate $Q = \mu U_0/\rho g H_0^2 \equiv 1/\epsilon^2 B$, and $S^\star = \gamma/\rho g H_0^2 \equiv S/\epsilon^2 B$. Figure 6(a) shows Cruickshank's data for $S^\star = 0.59$ and $Q = 41$ (open circles) and $Q = 144$ (solid circles) from his Fig. 24(m). Because Cruickshank nondimensionalized frequency and height using scales that did not change during the experiments, the trends of the points in Fig. 6(a) reflect directly the corresponding trends of the original (dimensional) measurements. Three features of the data are noteworthy: the folding frequency varies nonmonotonically with the height of fall; the minimum of the frequency-height curves shifts rightward with increasing Q; and curves for different Q cross each other.

All three features are explained by the scaling law (15). Figure 6(b) shows the frequencies predicted numerically for the same values of $S^\star$ and Q as in Fig. 6(a) (circles), together with those predicted by the scaling law (15) without surface tension (dashed lines for $Q = 41$, solid lines for $Q = 144$.) The left segments of the lines in Fig. 6(b) correspond to forced folding and the right segments correspond to free folding. The difference between the (solid, open) circles and the (solid, dashed) lines is a measure of the effect of surface tension, which is relatively small in all numerical solutions. The scaling law (15) for $S = 0$ can therefore be used to interpret numerical results with $S > 0$. The initial decrease of $f(H_0/g)^{1/2}$ with ϵ^{-1} is a direct consequence of the forced-folding scaling $f \sim U_1/L \approx U_0/L$, which is equivalent to $f(H_0/g)^{1/2} \sim \beta^{1/2}\epsilon$, where $\beta = g\rho^2 H_0^3/\mu^2$ ($= 7.6\times 10^{-4}$ in all experiments and numerical solutions in Fig. 6). Similarly, the rightward shift of the minimum with increasing Q is due to the fact that the forced-free transition point $\Pi \approx 3.92$ is equivalent to $\epsilon^{-1} \approx 3.92 Q^{1/4}$. Finally, curves with different Q cross because the dependence of the thickness H_1 in the folding region on the buoyancy number B is not a power law when B is finite. Using Eq. (14) with $B = \epsilon^{-2}Q^{-1}$ and $\hat{s}_1 = 0.88$ to rewrite the free-folding frequency (10), one finds

$$f(H_0/g)^{1/2} \sim \beta^{1/2} Q^{-1/2} \epsilon^{-5/2} [1 - 6.15\epsilon Q^{1/2} + 28.4\epsilon^2 Q + \cdots]^{-5/4}, \tag{16}$$

In the limit $\epsilon \to 0$, curves of $f(H_0/g)^{1/2}$ vs ϵ^{-1} are straight lines with slope 5/2 on a log-log plot, and curves for larger Q lie lower, as seen in the rightmost portion of Fig. 6(b). For larger ϵ, however, curves for larger Q are higher but have a smaller slope, due to the factor $[\cdots]^{-5/4}$ in Eq. (16). Curves for different Q therefore intersect at some value of ϵ^{-1}.

Although the trends of the numerical and experimental frequencies are quite similar, there remain quantitative differences between them of up to a factor of 2. There are at least two likely causes for this discrepancy. One is the effect of fluid inertia, which was neglected in the numerical code. Inertia is known to be important in the analogous phenomenon of the coiling of a viscous filament in the high-frequency limit [18,19], and may play a similar role in periodic folding of sheets. However, a more important cause is probably the significant three dimensionality of the laboratory experiments, where surface tension acting on the edges of the finite sheet causes its width to decrease substantially from top to bottom [Fig. 1(b)]. The effective values of ϵ^{-1} and Q in the folding region are therefore not the same as the nominal values at the top. Both inertial and three-dimensional effects could in principle be modeled using a more general set of viscous sheet equations, but that is beyond the scope of this study.

APPENDIX: MOTION OF THE CONTACT LINE

As extrusion proceeds, the sheet repeatedly comes into contact with the plate, forming a series of (fixed or mobile) contact lines. For the initial conditions I used, all contact lines are "tangent" ones for which the sheet's midsurface is locally horizontal. Let the position of the contact line be

$$\mathbf{r}_c(\ell,t) = x_c(t)\mathbf{x} + \left(-L + \frac{H(\ell,t)}{2}\right)\mathbf{y}. \tag{A1}$$

The vertical coordinate y is measured downward from the extrusion slot, so that the plate is at $y = -L$; the midsurface is a distance $H(\ell,t)/2$ above this. The lateral velocity of the contact point in the direction of the unit vector $\mathbf{s}(\ell,t)$ parallel to the plate is

$$U_c = \dot{x}_c(t)\mathbf{x}\cdot\mathbf{s}(\ell,t) \equiv \dot{x}_c(t)\cos\theta(\ell,t), \tag{A2}$$

where $\theta(\ell,t)=0$ or π depending on which way (right or left) the vector $\mathbf{s}(\ell,t)$ points. By evaluating evolution equation (3a) for $\mathbf{r}$ at $s=\ell$ and applying end conditions (6), one obtains

$$\frac{\partial\mathbf{r}}{\partial t}(\ell,t)+V(\ell,t)\mathbf{s}(\ell,t)-\frac{1}{2}\dot{H}(\ell,t)=0. \tag{A3}$$

By differentiating Eq. (A1) with respect to time and combining the result with Eqs. (A2) and (A3), one obtains

$$\dot{\ell}=V(\ell,t)+U_c \equiv U_0+\int_0^{\ell}\Delta(s,t)\,ds+U_c. \tag{A4}$$

Equation (A4) shows that the sheet's length changes due to extrusion of fluid at speed U_0, distributed stretching along the sheet, and motion of the contact line at speed U_c, which lengthens the sheet if $U_c>0$ (advancing contact line) and shortens it if $U_c<0$ (retreating contact line).

Consider now evolution equation (3b) for θ, which when evaluated at $s=\ell$ yields

$$\frac{\partial\theta}{\partial t}(\ell,t)+V(\ell,t)K(\ell,t)=0. \tag{A5}$$

However, because $\theta(\ell,t)$ is a constant ($=0$ or π),

$$\frac{\partial\theta}{\partial t}(\ell,t)+\dot{\ell}\frac{\partial\theta}{\partial s}(\ell,t)\equiv\frac{\partial\theta}{\partial t}(\ell,t)+\dot{\ell}K(\ell,t)=0, \tag{A6}$$

which together with Eqs. (A4) and (A5) implies

$$U_cK(\ell,t)=0. \tag{A7}$$

Therefore the contact line can move if and only if the sheet's curvature vanishes there. Consider first the case $K(\ell,t)\neq 0$. Because the curvature of the sheet is nonzero at a newly formed tangent contact line, such a contact line will not move initially. Two separate cases must be distinguished, depending on whether the absolute curvature $|K(\ell,t)|$ at the contact point is increasing or decreasing. A general expression for the rate of change of the curvature at the contact line can be found using Eq. (A4) and evolution equation (3c) for K, and is

$$\dot{K}(\ell,t)=U_c\frac{\partial K}{\partial s}(\ell,t)+\frac{\partial\omega}{\partial s}(\ell,t)-K(\ell,t)\Delta(\ell,t). \tag{A8}$$

If $\dot{K}(\ell,t)$ and $K(\ell,t)$ have the same sign, the absolute curvature at the contact line is increasing, i.e., the portion of the sheet near the contact line is bending away from the plate. Such a contact line is "pinned," because the sheet once laid down cannot be peeled away from the plate again. If, however, $\dot{K}(\ell,t)$ and $K(\ell,t)$ have opposite signs, the sheet is bending towards the plate and the absolute curvature is decreasing. Such a "relaxing" contact line will eventually become a "mobile" one when the curvature drops to zero. The subsequent speed of the contact line is given by Eq. (A8) with $K(\ell,t)=\dot{K}(\ell,t)=0$, or

$$U_c=-\frac{d\omega}{dK}(\ell,t). \tag{A9}$$

This research was supported by the Centre Nationale de la Recherche Scientifique (France). I thank A. Boudaoud, M. Brenner, A. Davaille, H. Huppert, J. Lister, L. Mahadevan, H. Stone, and M. G. Worster for helpful discussions. The apparatus used in the preparation of Fig. 1 was constructed by Y. Gambelin.

[1] M.F. Tome and S. McKee, Int. J. Numer. Methods Fluids **29**, 705 (1999).
[2] J.R.A. Pearson, *Mechanics of Polymer Processing* (Elsevier, Amsterdam, 1985).
[3] R.W. Griffiths and J.S. Turner, Geophys. J. **95**, 397 (1988).
[4] G.I. Taylor, *Proceedings of the Twelfth International Congress of Applied Mechanics* (Springer, Berlin, 1968).
[5] J.O. Cruickshank, Ph.D. thesis, Iowa State University, 1980.
[6] J.O. Cruickshank and B.R. Munson, J. Fluid Mech. **113**, 221 (1981).
[7] J.O. Cruickshank, J. Fluid Mech. **193**, 111 (1988).
[8] A.L. Yarin and B.M. Tchavdarov, J. Fluid Mech. **307**, 85 (1996).
[9] M. Skorobogatiy and L. Mahadevan, Europhys. Lett. **52**, 532 (2000).
[10] S.M. Suleiman and B.R. Munson, Phys. Fluids **24**, 1 (1981).
[11] T.B. Benjamin and T. Mullin, J. Fluid Mech. **195**, 523 (1988).
[12] R. da Silveira, S. Chaieb, and L. Mahadevan, Science **287**, 1468 (2000).
[13] A. Boudaoud and S. Chaieb, Phys. Rev. E **64**, 050601(R) (2001).
[14] N.M. Ribe, J. Fluid Mech. **433**, 135 (2001).
[15] N.M. Ribe, J. Fluid Mech. **457**, 255 (2002).
[16] J.D. Buckmaster, A. Nachman, and L. Ting, J. Fluid Mech. **69**, 1 (1975).
[17] W.H. Press, S.A. Teukolsky, W.T. Vetterling, and B.P. Flannery, *Numerical Recipes in Fortran 77: The Art of Scientific Computing*, 2nd ed. (Cambridge University Press, Cambridge, 1996).
[18] L. Mahadevan, W.S. Ryu, and A.D.T. Samuel, Nature (London) **392**, 140 (1998).
[19] L. Mahadevan, W.S. Ryu, and A.D.T. Samuel, Nature (London) **403**, 502 (2000).